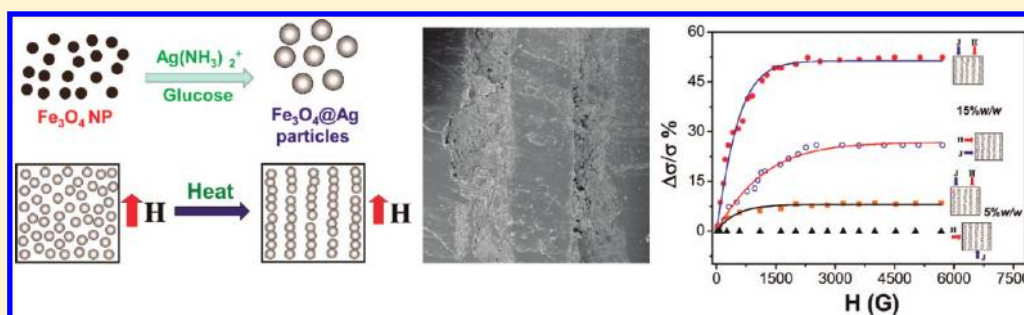


Anisotropic Magnetoresistance and Piezoresistivity in Structured  $\text{Fe}_3\text{O}_4$ -Silver Particles in PDMS Elastomers at Room TemperatureJosé L. Mietta,<sup>†</sup> Mariano M. Ruiz,<sup>†</sup> P. Soledad Antonel,<sup>†</sup> Oscar E. Perez,<sup>‡</sup> Alejandro Butera,<sup>||</sup> Guillermo Jorge,<sup>§</sup> and R. Martín Negri<sup>\*,†</sup><sup>†</sup>Instituto de Química Física de Materiales, Ambiente y Energía (INQUIMAE), Departamento de Química Inorgánica, Analítica y Química Física, <sup>‡</sup>Departamento de Industrias, and <sup>§</sup>Departamento de Física, Facultad de Ciencias Exactas y Naturales, Universidad de Buenos Aires<sup>||</sup>Centro Atómico Bariloche, Comisión Nacional de Energía Atómica, Argentina, and Instituto Balseiro, Universidad Nacional de Cuyo, Bariloche, Río Negro, Argentina

## Supporting Information



**ABSTRACT:** Magnetorheological elastomers, MREs, based on elastic organic matrices displaying anisotropic magnetoresistance and piezoresistivity at room temperature were prepared and characterized. These materials are dispersions of superparamagnetic magnetite forming cores of aggregated nanoparticles inside silver microparticles that are dispersed in an elastomeric polymer (poly(dimethylsiloxane), PDMS), curing the polymer in the presence of a uniform magnetic field. In this way, the elastic material becomes structured as the application of the field induces the formation of filaments of silver-covered inorganic material agglomerates (needles) aligned in the direction of the field (parallel to the field). Because the magnetic particles are covered with silver, the MREs are not only magnetic but also electrical conductors. The structuration induces elastic, magnetic, and electrical anisotropic properties. For example, with a low concentration of particles in the elastic matrix (5% w/w) it is possible to obtain resistances of a few ohms when measured parallel to the needles or several megaohms in the perpendicular direction. Magnetite nanoparticles ( $\text{Fe}_3\text{O}_4$  NP) were synthesized by the coprecipitation method, and then agglomerations of these NPs were covered with Ag. The average size of the obtained magnetite NPs was about 13 nm, and the magnetite-silver particles, referred to as  $\text{Fe}_3\text{O}_4@Ag$ , form micrometric aggregates (1.3  $\mu\text{m}$ ). Nanoparticles, microparticles, and the MREs were characterized by XRD, TEM, SEM, EDS, diffuse reflectance, voltammetry, VSM, and SQUID. At room temperature, the synthesized magnetite and  $\text{Fe}_3\text{O}_4@Ag$  particles are in a superparamagnetic state ( $T_B = 205$  and 179 K at 0.01 T as determined by SQUID). The elastic properties and Young's modulus of the MREs were measured as a function of the orientation using a texture analysis device. The magnetic anisotropy in the MRE composite was investigated by FMR. The electrical conductivity of the MRE ( $\sigma$ ) increases exponentially when a pressure,  $P$ , is applied, and the magnitude of the change strongly depends on what direction  $P$  is exerted (anisotropic piezoresistivity). In addition, at a fixed pressure,  $\sigma$  increases exponentially in the presence of an external magnetic field ( $H$ ) only when the field  $H$  is applied in the collinear direction with respect to the electrical flux,  $J$ . Excellent fits of the experimental data  $\sigma$  versus  $H$  and  $P$  were achieved using a model that considers the intergrain electron transport where an  $H$ -dependent barrier was considered in addition to the intrinsic intergrain resistance in a percolation process. The  $H$ -dependent barrier decreases with the applied field, which is attributed to the increasing match of spin-polarization in the silver covers between grains. The effect is anisotropic (i.e., the sensitivity of the magnetoresistive effect is dependent on the relative orientation between  $H$  and the current flow  $J$ ). In the case of  $\text{Fe}_3\text{O}_4@Ag$ , when  $H$  and  $J$  are parallel to the needles in the PDMS matrix, we obtain changes in  $\sigma$  up to 50% for fields of 400 mT and with resistances on the order of 1–10  $\Omega$ . Magnetoresistive and magnetoelastic properties make these materials very interesting for applications in flexible electronics, electronic skins, anisotropic pressure, and magnetic field sensors.

## 1. INTRODUCTION

Magnetorheological elastomers are of particular interest for applications in devices, particularly in flexible electronics, which

Received: December 7, 2011

Revised: March 26, 2012

is a field of high activity at present, integrating research in basic materials science and microelectronics for technological innovations such as electronic skins,<sup>1</sup> full-flexible integrated pressure sensors,<sup>2</sup> pressure map sensors,<sup>3</sup> tactile sensors,<sup>4</sup> low-power flexible transistors,<sup>5</sup> and robotic fingers.<sup>5,6</sup> As a difference with respect to magnetofluids that had been extensively studied,<sup>7–9</sup> magnetorheological elastomers (MRE) have not yet been systematically investigated. A magnetorheological elastomer is defined as a material composed of magnetic particles, nanotubes, or nanowires aligned in a polymer medium by exposure to a magnetic field,<sup>10–12</sup> thus having elastic and/or magnetic anisotropic properties<sup>13–20</sup> that can be used to implement magnetic field sensors<sup>21</sup> or electromagnetic energy convertor composites.<sup>22</sup> Although many magnetic compounds can be used as fillers, magnetite is the most used in MRE. Nevertheless, Kchit and Bossis<sup>19</sup> developed nickel-based MRE for pressure sensors, and we have recently investigated the elastic and magnetic behavior of MRE using  $\text{CoFe}_2\text{O}_4$  nanoparticles in PDMS.<sup>23</sup> The MRE can be used to make anisotropic pressure sensors when using fillers that are simultaneously magnetic and electrically conductive because the elastic properties depend on the direction of the applied stress (e.g., Young's modulus is higher in the direction of the aligned particles), which induces anisotropic electrical conduction through the preferential percolation of the conductive particles. This possibility was explored by Kchit and Bossis<sup>19</sup> and constitutes an interesting improvement over the commonly used isotropic carbon-elastomer composites whose characteristic piezoresistivity (variation of the electrical conductivity with the strain) has been systematically studied and used to implement pressure sensors and whose dependence on the strain was modeled under different conditions,<sup>24,25</sup> including a model developed in our group for a high filler concentration.<sup>26</sup>

In spite of the mentioned work, the research and development of MREs for flexible devices having anisotropic low-field magnetoresistance (LFMR) at room temperature have not yet been explored, even though LFMR effects in MREs have a huge potential for implementing new elastomeric connectors (such as zebra connectors) or in organic-based spintronic devices.<sup>27–30</sup> In the case of magnetite ( $\text{Fe}_3\text{O}_4$ ), there are few reports of LFMR at room temperature for  $\text{Fe}_3\text{O}_4$  films,<sup>31</sup> but there are no studies in MRE to our knowledge.

In the present work, MRE materials displaying both anisotropic piezoresistivity and LFMR effects at room temperature are presented on the basis of superparamagnetic  $\text{Fe}_3\text{O}_4$  nanoparticles (13 nm) that are agglomerated inside silver shells, thus forming microparticles (1.3  $\mu\text{m}$ , referred to as  $\text{Fe}_3\text{O}_4@\text{Ag}$ ) dispersed in a PDMS matrix and cured in the presence of a uniform magnetic field. In this manner, anisotropically structured MREs were obtained with the formation of macroscopic needles ( $\sim 1\text{--}3$  mm length) composed of groups of the  $\text{Fe}_3\text{O}_4@\text{Ag}$  microparticles. Measurements of the magnetic properties, elastic properties (including Young's modulus), piezoresistivity, and low-field magnetoresistance of these MRE materials are presented and discussed.

## 2. MATERIALS AND METHODS

**2.1. Synthesis of  $\text{Fe}_3\text{O}_4$  Nanoparticles.** The chemical coprecipitation method was used for the synthesis of  $\text{Fe}_3\text{O}_4$  nanoparticles. Adapting from Antonel et al.,<sup>23</sup> 22.25 mL of a solution mixture of 0.450 M  $\text{FeCl}_3\cdot 6\text{H}_2\text{O}$  and 0.225 M  $\text{FeCl}_2\cdot 4\text{H}_2\text{O}$  (2:1), in 0.4 M HCl, was added drop by drop to 200 mL of 1.5 M NaOH, previously adjusted to pH 12, under high-speed stirring. The synthesis

temperature (60 °C) was controlled by a water-jacketed reaction vessel with a circulating thermostatic bath. The precipitation of dark-brown  $\text{Fe}_3\text{O}_4$  nanoparticles occurred immediately, and both high-speed stirring and the desired temperature were maintained during the addition of the cationic mixture. The obtained precipitates were vigorously stirred at the desired temperature for 2 h. The synthesis procedure described in the preceding text was performed under a nitrogen atmosphere to prevent the oxidation of Fe(II) ions.

Then  $\text{Fe}_3\text{O}_4$  nanoparticles were separated from the reaction medium by centrifugation at approximately 12 000g for 20 min. The obtained precipitates were washed with Milli-Q water, and further washing and centrifugation cycles (always at 12 000g) were repeated until the pH of the supernatant was nearly 7 (approximately 10 cycles of washing and centrifugation). It was confirmed by XRD that 10 cycles of washing and centrifugation also eliminate NaCl that was present in the reaction medium because of the solutions used in the synthesis. The characteristic peaks of NaCl appear in the diffractograms if fewer cycles of washing/centrifugation are performed. Finally, the  $\text{Fe}_3\text{O}_4$  nanoparticles were dried in a vacuum oven at 40 °C for 24 h.

**2.2. Synthesis of  $\text{Fe}_3\text{O}_4@\text{Ag}$  Microparticles.** Several methods have been reported for obtaining nanoparticle agglomerates with metals.<sup>32–35</sup> Here the objective was to obtain electrically conductive agglomerates ( $\text{Fe}_3\text{O}_4@\text{Ag}$ ) that also increase the stability of the magnetic particles for periods of at least 8 months by preventing oxidation. The synthesis protocol, promoting the reduction of Ag(I) ions adsorbed onto  $\text{Fe}_3\text{O}_4$  particles, was adapted from Mandal et al.,<sup>33</sup> Iglesias-Silva et al.,<sup>34</sup> and Yin et al.<sup>35</sup> Three different sets, referred as A, B, and C, were prepared to compare synthesis conditions. Dispersions of  $\text{Ag}^+$  and  $\text{Fe}_3\text{O}_4$  in a 10:1 molar ratio were sonicated for 30 min in the three sets.  $\text{AgNO}_3$  was used for set A, and  $\text{Ag}(\text{NH}_3)_2^+$  was used for sets B and C. Then sets A and B were heated in a water bath at 50 °C for 20 min with slow stirring, and set C was stirred for 20 min at room temperature. In the next step, a 0.4 M glucose monohydrate solution was added drop by drop to the  $\text{Fe}_3\text{O}_4\text{--Ag}^+$  suspension. For set A, stirring was continued for 20 h, whereas for sets B and C stirring was continued for only 1 h. As the particles are gradually covered with silver, the black  $\text{Fe}_3\text{O}_4$  particles turn brownish (set A) and light brown (sets B and C). These magnetite–silver particles were separated out from the solution by magnetization and then by centrifugation (approximately six cycles of washing and centrifugation). After the particles were separated, the decanted supernatant liquid was fully transparent. For comparison purposes, silver particles (reddish orange) were produced in a separate batch using the same experimental conditions for each set.

**2.3. Preparation of PDMS- $\text{Fe}_3\text{O}_4$  and PDMS- $\text{Fe}_3\text{O}_4@\text{Ag}$  MREs.** The details of the preparation of PDMS-NPs structured MREs have been described in previous work.<sup>23</sup> Briefly, a PDMS base and a cross-linking agent (Sylgard 184, Dow Corning) were mixed in a proportion of 10:1 w/w at room temperature and then loaded with the magnetic nanoparticles. PDMS and fillers were weighed during mixing on an analytical balance, homogenized, and placed at room temperature in a vacuum oven for about 2 h until the complete absence of any air bubbles was attained.

Specifically, composites with 5 and 15% w/w of the  $\text{Fe}_3\text{O}_4$  nanoparticles were prepared, and the same percentage of  $\text{Fe}_3\text{O}_4$  in the composite was considered for the  $\text{Fe}_3\text{O}_4@\text{Ag}$  composites. The still fluid samples were incorporated into a specially designed cylindrical mold (1 cm diameter  $\times$  3 cm length) and placed in between the magnetic poles of a Varian low impedance electromagnet (model V3703) that provides highly homogeneous steady magnetic fields. The mold was rotated at 30 rpm and heated to  $75 \pm 5$  °C in the presence of a uniform magnetic field (0.3 T) for 4 h to obtain a cured material. Controls without applying the magnetic field were performed. More details are provided in Antonel et al.<sup>23</sup>

**2.4. Instrumentation.** X-ray powder diffraction analysis (XRD) was performed with a Philips X-Pert diffractometer using Cu K $\alpha$  radiation ( $\lambda = 0.154056$  nm), and the average size of the  $\text{Fe}_3\text{O}_4$  crystallites was determined by the Debye–Scherrer equation. A transmission electron microscope (TEM, Philips EM 301) was employed to examine the morphology and size of the  $\text{Fe}_3\text{O}_4$

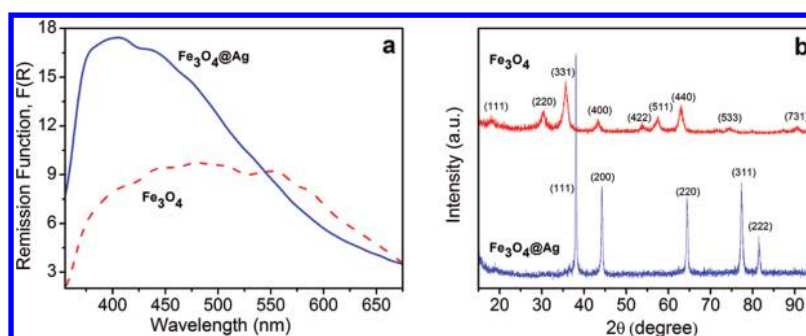


**Figure 1.** (a) Remission function as a function of wavelength for  $\text{Fe}_3\text{O}_4@Ag$  microparticles, set B (—) and  $\text{Fe}_3\text{O}_4$  nanoparticles (---). (b) XRD patterns of the  $\text{Fe}_3\text{O}_4$  nanoparticles and  $\text{Fe}_3\text{O}_4@Ag$  particles (set B).

nanoparticles, whose size distribution was determined in each case by counting 260 particles. A similar procedure was performed for  $\text{Fe}_3\text{O}_4@Ag$  microparticles using SEM images, counting 280 particles. The morphology of the  $\text{Fe}_3\text{O}_4@Ag$  agglomerates,  $\text{Fe}_3\text{O}_4$ -PDMS and  $\text{Fe}_3\text{O}_4@Ag$ -PDMS composites, was studied using a field emission scanning electron microscope (FESEM, Zeiss Supra 40 Gemini). Energy-dispersive X-ray spectroscopy (EDS) experiments were performed with the same equipment.

A spectrophotometer (UV3101PC, Shimadzu) was used for the reflectance measurements. Barium sulfate was employed as a white reference standard to adjust the 100% reflectance level. Diffuse reflectance was recorded as a function of wavelength between 300 and 700 nm. The remission function,  $F(R)$ , was calculated as described by Yaryura et al.<sup>36</sup> FTIR spectra were recorded with Nicolet 8700 equipment incorporating the samples into KBr pellets.

A LakeShore 7400 vibrating sample magnetometer (VSM) was used to record magnetization curves at room temperature. Zero field cooling (ZFC) and field cooling (FC) magnetization curves were recorded in a superconducting quantum interference device (SQUID) magnetometer (Quantum Design MPMS XL). The following data treatment was performed to obtain the average blocking temperature. The ZFC curve was subtracted from the FC, and the derivative of that curve was calculated and normalized to area one. This curve was used as the density probability function for the blocking temperature. Then the average blocking temperature,  $T_B$ , was calculated. This procedure is similar to that reported by Knobel et al.<sup>37</sup> Ferromagnetic resonance (FMR) spectra of the MRE composites were recorded with a Bruker ESP-300 spectrometer at room temperature.

The analysis of elasticity and Young's modulus determination were performed using a Stable Microsystems TA-XT2i texture analyzer, which compresses the sample at a constant speed (100  $\mu\text{m/s}$ ) in the range between 8 and 30% of the initial thickness.<sup>23,26</sup> Specific details of the elastic measurements and data treatment are described in our previous work.<sup>23,26</sup> Samples for elasticity analysis were prepared by cutting the cured composites in the transversal and longitudinal directions with respect to the applied magnetic field during the curing process. A specially designed device (described in Antonel et al.<sup>23</sup>) was used to cut the cured composites in order to obtain pieces of equal thickness (3 mm) and similar areas (0.78 and 0.83  $\text{cm}^2$ ) in both directions.

A TEQ 4 (Argentina) potentiostat was used for the voltammetry measurements for determinations of the  $I$ – $V$  characteristic curves of the powders. Powders of the studied materials ( $\text{Fe}_3\text{O}_4$  and  $\text{Fe}_3\text{O}_4@Ag$ ) were placed inside a plastic capillary tube (2 mm diameter) that was vertically placed on an electronic balance. Metallic cylinders were introduced from both sides of the capillary tube and compressed using a designed bridge positioned above the balance, which allows us to change the pressure applied to the powder. The metallic cylinders were connected to the potentiostat in order to record the  $I$ – $V$  (dc, between –3000 and +3000 mV) characteristic curves of the powders at each applied pressure.

## 2.5. Piezoresistivity and Magnetoresistance of PDMS MREs.

A specially designed device was used to measure the piezoresistivity of PDMS- $\text{Fe}_3\text{O}_4@Ag$  MRE. The device includes two plastic plates that compress the samples and allow the required force to be applied. The

force during compression was measured by a force sensor, and the voltammetry was simultaneously recorded using the TQ4 equipment at different pressures.

The device for measuring magnetoresistance consists of placing the setup described above between the pole pieces of an electromagnet that generates a uniform magnetic field. A gaussmeter (Group3 DTM-133 digital teslameter) was used to test the intensity of the magnetic field. To measure the electrical resistivity in the MRE samples for different values of  $H$ , the current flux through the sample was measured under different intensities of  $H$  by applying an arbitrary and constant pressure between two copper electrodes (ferromagnetic electrodes must be avoided).

## 3. RESULTS

### 3.1. Chemical and Morphological Characterization.

Figure 1a shows the remission function spectra of both  $\text{Fe}_3\text{O}_4$  and  $\text{Fe}_3\text{O}_4@Ag$  (set B) powders measured by diffuse reflectance. The apparition of an intense band with a peak at 400 nm for the  $\text{Fe}_3\text{O}_4@Ag$  powders, which is assigned to the Ag plasmon formed on the surface of the semiconductor, can clearly be seen.<sup>34</sup> The associated change of color can be observed by the naked eye, and pictures are shown in the Supporting Information (Figure S1). X-rays diffractograms of powders with and without silver are also presented in Figure 1b, where the corresponding peaks of an inverse spinel are observed for  $\text{Fe}_3\text{O}_4$ , as expected (ICDD 19-0629). In the case of  $\text{Fe}_3\text{O}_4@Ag$  powders, the peaks of  $\text{Fe}_3\text{O}_4$  are not observed but only those of Ag (ICDD 00-004-0783), which is clear evidence that the  $\text{Fe}_3\text{O}_4$  nanoparticles are covered by silver as indicated by Mandal et al.,<sup>33</sup> Iglesias-Silva et al.,<sup>34</sup> and Wang et al.<sup>38</sup> The FTIR spectra (not shown) are also in agreement with the picture in which the magnetite particles are not exposed but distributed in the cores of silver particles (the structure referred as  $\text{Fe}_3\text{O}_4@Ag$  particles in this work) because the peak at 413  $\text{cm}^{-1}$  (stretching frequency for the Fe–O bond) vanished completely for  $\text{Fe}_3\text{O}_4@Ag$  with respect to the uncovered particles, which has been mentioned as an indication of the silver coating formation.<sup>33</sup>

The size and morphology of the  $\text{Fe}_3\text{O}_4$  and  $\text{Fe}_3\text{O}_4@Ag$  particles were determined by TEM and SEM, respectively (Figure S2, Supporting Information). The histograms were obtained by counting 260 and 280 particles in each case. The maximum in the distribution is at 13 nm for the  $\text{Fe}_3\text{O}_4$  nanoparticles. The size of the crystallite domains was calculated by Debye–Scherrer using XRD, obtaining a diameter of  $14 \pm 2$  nm, which is in excellent agreement with the maximum in the nanoparticles size distribution. For the  $\text{Fe}_3\text{O}_4@Ag$  microparticles, the maximum in the distribution (SEM) is at 1.3  $\mu\text{m}$ .



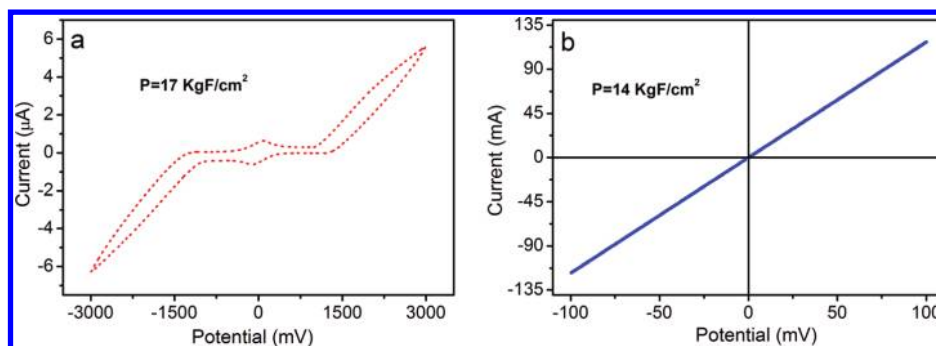


**Figure 2.** (a) Cyclic voltammograms for  $\text{Fe}_3\text{O}_4$  nanoparticles at  $P = 17 \text{ kgF/cm}^2$  and room temperature. The scan rate is  $50 \text{ mV}\cdot\text{s}^{-1}$ . (b) Cyclic voltammograms for  $\text{Fe}_3\text{O}_4\text{@Ag}$  particles (set B) at  $P = 14 \text{ kgF/cm}^2$  and room temperature. The scan rate is  $1 \text{ mV}\cdot\text{s}^{-1}$ .

EDS results confirmed the expected stoichiometry of  $\text{Fe}_3\text{O}_4$  nanoparticles and indicated the following Ag percentage for  $\text{Fe}_3\text{O}_4\text{@Ag}$  samples prepared with the three protocols (section 2.1): 32, 82, and 65% w/w for A–C, respectively. Therefore, the particles used for MRE preparation are those obtained with protocol B, which resulted in the higher silver percentage.

**3.2. Electrical Characterization of the  $\text{Fe}_3\text{O}_4$  and  $\text{Fe}_3\text{O}_4\text{@Ag}$  Powders.** Figure 2a shows a cyclic voltammogram of the  $\text{Fe}_3\text{O}_4$  nanoparticles when compressed at room temperature ( $25^\circ\text{C}$ ) and with a fixed pressure ( $17 \text{ kgF/cm}^2$ ) in the setup described in section 2.4. We observe in this figure a typical voltammogram of a semiconductor with thresholds at  $\pm 1100$  and  $-1100$  mV, which is independent of the applied pressure in the considered range ( $0$ – $100 \text{ kgF/cm}^2$ , results not shown), and currents on the order of a few microamps. Low redox peaks, probably associated with the  $\text{Fe(II)/Fe(III)}$  couple, appear near  $\pm 250$  mV and are also independent of the pressure.

Figure 2b shows the respective voltammogram for the  $\text{Fe}_3\text{O}_4\text{@Ag}$  microparticles (set B) under similar conditions. We now clearly observe ohmic behavior (over the entire pressure range) with currents on the order of  $100 \text{ mA}$ , which are  $10^5$  times larger than that of uncovered magnetite. The resistivity of the powder decreases with pressure because of an increase in the number of electric contacts between particles during compression.

These results confirm that we obtained silver-covered particles with ohmic behavior and low resistivity, which is consistent with the metallic nature of the coating, one of the initially proposed objectives of this work.

**3.3. Magnetic Characterization of the  $\text{Fe}_3\text{O}_4$  and  $\text{Fe}_3\text{O}_4\text{@Ag}$  Powders.** At room temperature ( $298 \text{ K}$ ),  $\text{Fe}_3\text{O}_4$  NPs and all of the  $\text{Fe}_3\text{O}_4\text{@Ag}$  particles are in a superparamagnetic state as determined by VSM (Figure 3a). The superparamagnetic behavior at  $298 \text{ K}$  and below the Curie temperature,  $T_C$  ( $858 \text{ K}$ ), is consistent with the small size of the nanoparticles ( $13 \text{ nm}$ ), indicating that the diameter of the nanoparticles is below the critical diameter in which the particles are magnetic single domains. The saturation magnetization per gram of material ( $M_S$ ) decreases when the silver percentage increases, as expected. The average blocking temperatures ( $T_B$ ), related to the transition from superparamagnetic to a blocked state during cooling, were determined by SQUID experiments (ZFC and FC curves shown in Figure 3b,c). The obtained values of  $T_B$  at  $0.01 \text{ T}$  were  $205 \text{ K}$  for  $\text{Fe}_3\text{O}_4$  and  $179 \text{ K}$  for  $\text{Fe}_3\text{O}_4\text{@Ag}$ , which confirms that at  $298 \text{ K}$  the materials are in a superparamagnetic state. Although Mandal et al.<sup>33</sup> attributed the decrease in  $T_B$

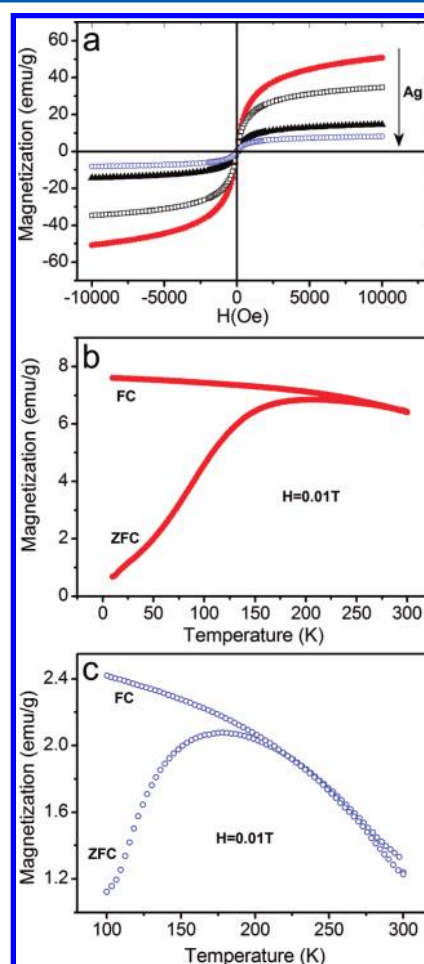


**Figure 3.** (a) Magnetic hysteresis curves at  $25^\circ\text{C}$  for  $\text{Fe}_3\text{O}_4$  nanoparticles ( $-\bullet-$ ) and  $\text{Fe}_3\text{O}_4\text{@Ag}$  microparticles synthesized under different conditions: set A ( $-\square-$ ), set C ( $-\blacktriangle-$ ), and set B ( $-\circ-$ ). (b) ZFC and FC magnetization vs temperature curves ( $H = 0.01 \text{ T}$ ) for the  $\text{Fe}_3\text{O}_4$  nanoparticles. (c) ZFC and FC magnetization vs temperature curves ( $H = 0.01 \text{ T}$ ) for the  $\text{Fe}_3\text{O}_4\text{@Ag}$  particles, set B.

with the increase in Ag to an increase in the internanoparticle separation (lowering the average magnetic dipole–dipole interaction), that mechanism seems to be more appropriate when each of the individual nanoparticles is covered with a silver shell, which is not the present case. Therefore, the observed decrease in  $T_B$  with Ag is perhaps due to the interaction between Ag atoms and magnetite nanoparticles,

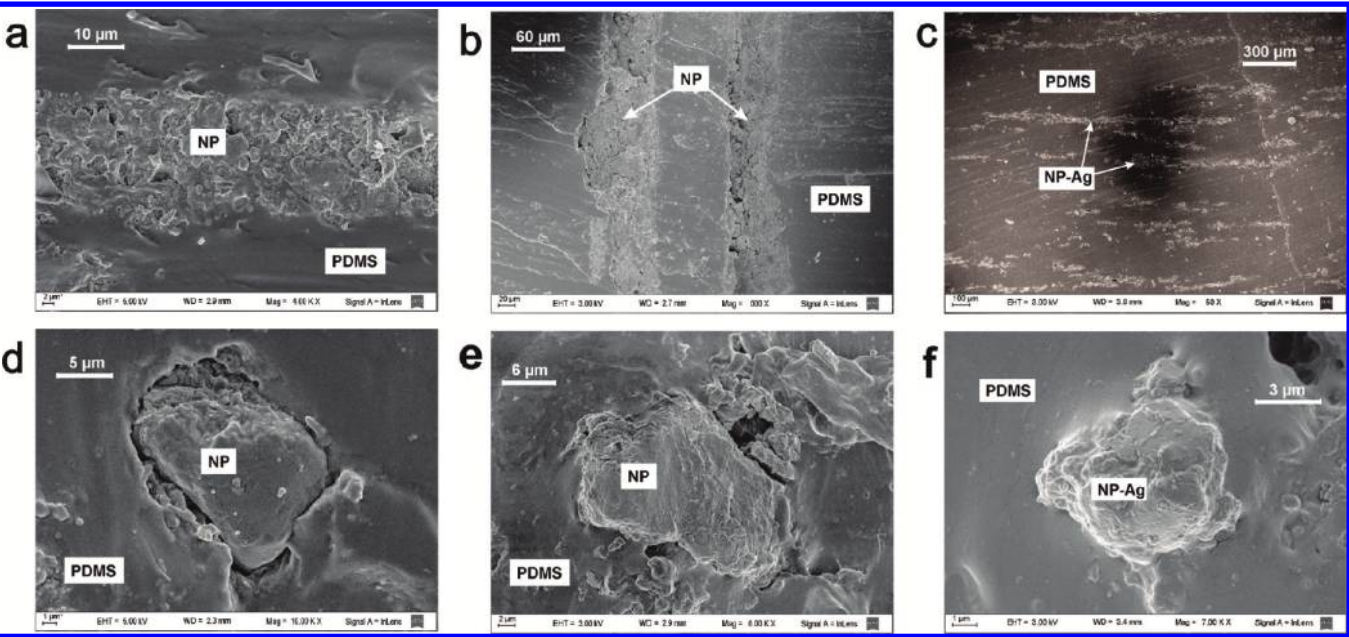


**Figure 4.** SEM images of the structured PDMS-Fe<sub>3</sub>O<sub>4</sub> and PDMS-Fe<sub>3</sub>O<sub>4</sub>@Ag composites. Lateral view of inorganic needles: (a) 5% w/w of Fe<sub>3</sub>O<sub>4</sub>, (b) 15% w/w of Fe<sub>3</sub>O<sub>4</sub>, and (c) 5% w/w of Fe<sub>3</sub>O<sub>4</sub>@Ag. Top view of inorganic needles: (d) 5% w/w of Fe<sub>3</sub>O<sub>4</sub>, (e) 15% w/w of Fe<sub>3</sub>O<sub>4</sub>, and (f) 5% w/w of Fe<sub>3</sub>O<sub>4</sub>@Ag. NP indicates Fe<sub>3</sub>O<sub>4</sub> nanoparticles, and NP-Ag indicates Fe<sub>3</sub>O<sub>4</sub>@Ag particles.

**Table 1. Morphological Average Properties of Different MRE Composites**

composite	average diameter of needles, $\mu\text{m}$	average length of needles, mm	density of needles, needles/ $\text{mm}^3$	percentage volume fraction occupied by the needles, $\Phi_v$ (%)
PDMS-Fe <sub>3</sub> O <sub>4</sub> 15% w/w	51	3.0	12.3	7.5
PDMS-Fe <sub>3</sub> O <sub>4</sub> 5% w/w	20	3.0	14.8	1.4
PDMS-Fe <sub>3</sub> O <sub>4</sub> @Ag 15% w/w	15	0.9	90.3	1.4
PDMS-Fe <sub>3</sub> O <sub>4</sub> @Ag 5% w/w	10	1.3	9.4	0.1

leading to a modification of magnetic parameters such as the anisotropy constant.

The percentage of Ag in the different Fe<sub>3</sub>O<sub>4</sub>@Ag samples can be estimated from the comparison of the  $M_s$  values with the  $M_s$  for Fe<sub>3</sub>O<sub>4</sub> nanoparticles, obtained from Figure 3a. Silver percentages recovered by this method were 31, 84, and 67% w/w for protocols A–C, respectively, in excellent agreement with the value obtained by EDS analysis (section 3.1).

**3.4. MRE PDMS Composites: Morphology and Magnetic Properties.** The formation of macroscopic needles of inorganic material observed by the naked eye was obtained after curing in the presence of a magnetic field under the conditions and setup described in section 2.3. The formation of needles was observed when Fe<sub>3</sub>O<sub>4</sub> or Fe<sub>3</sub>O<sub>4</sub>@Ag was used as fillers, but only in the case of curing PDMS in the presence of an applied field. The needles are formed when using Fe<sub>3</sub>O<sub>4</sub> or Fe<sub>3</sub>O<sub>4</sub>@Ag. SEM images of the needles in the cured material are shown in Figure 4a–f. A lateral view of the needles is presented in Figure 4a–c, whereas top views are presented in Figure 4d–f.

The average diameter, length, density, and volume fraction of the needles were calculated from the SEM images and are shown in Table 1. A panoramic view of the SEM images for the PDMS-Fe<sub>3</sub>O<sub>4</sub>@Ag composite with a relatively large loading (15% w/w) is presented in Figure S3 (Supporting Information), where several needles dispersed in the PDMS can be observed. About 320 SEM images were used to estimate the parameters indicated in Table 1 (under the conditions illustrated in Figure 4a–f and Figure S3 of the Supporting

Information) at several magnifications (from 50 to 6000 $\times$ ). A voltages (EHT) of 5 kV and magnifications of 100 $\times$  (3300 pixels/cm) and 300 $\times$  (9800 pixels/cm) were typical conditions for determining the average chain length, whereas 3 kV and 4000 $\times$  (40 pixels/ $\mu\text{m}$ ) were used to obtain the average chain diameter.

In all cases, the diameter of the needles increases when the mass of filler increases. The volume fraction of the needles ( $\Phi_v$ ) also increases as expected. The average values of the diameter and length are larger for PDMS-Fe<sub>3</sub>O<sub>4</sub> than for PDMS-Fe<sub>3</sub>O<sub>4</sub>@Ag composites, probably because of the larger magnetic interaction in PDMS-Fe<sub>3</sub>O<sub>4</sub>.

The  $T_B$  values of the MRE composites for different orientations of  $H$  with respect to the needles were calculated from the data shown in Figure 5c,d using the data analysis described in section 2.4. For 15% w/w PDMS-Fe<sub>3</sub>O<sub>4</sub>,  $T_B = 238$  and 211 K were obtained for the parallel and perpendicular directions (with reference to the needles), respectively. For 15% w/w PDMS-Fe<sub>3</sub>O<sub>4</sub>@Ag,  $T_B = 185$  and 169 K were obtained in the respective cases. This analysis shows that  $T_B$  is always lower when the magnetic field is applied in the direction perpendicular to the needles (for a fixed concentration of particles). This is reasonable because it requires a lower temperature to produce the transition from the blocked to the superparamagnetic state when the magnetic field is applied in the direction perpendicular to the needles because of a decrease in the dipole–dipole interaction in that configuration. Whatever the direction of the applied field,  $M_s$  and  $T_B$  are larger for PDMS-Fe<sub>3</sub>O<sub>4</sub> than for PDMS-Fe<sub>3</sub>O<sub>4</sub>@Ag MRE, an identical

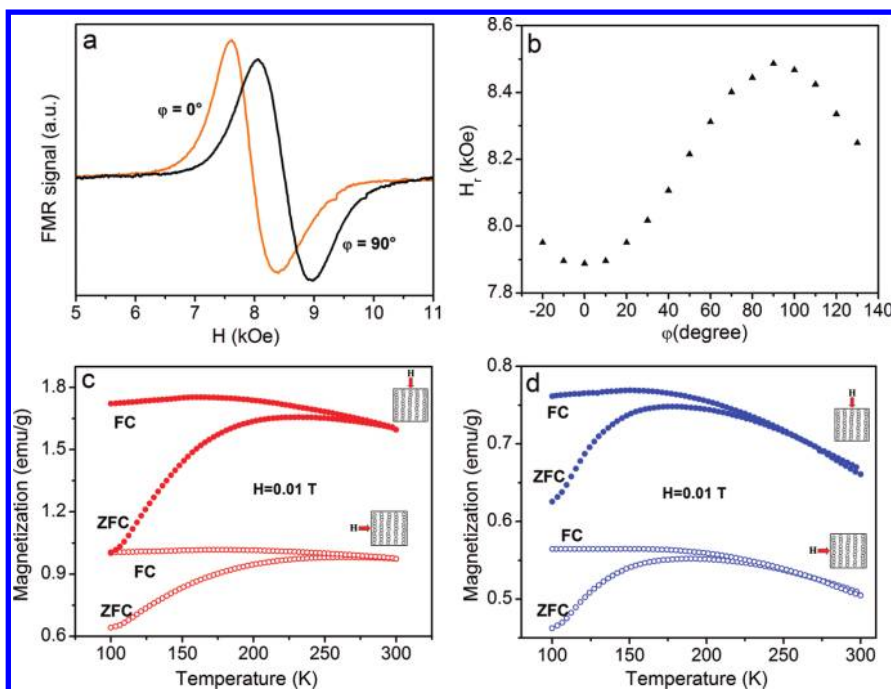


**Figure 5.** (a) FMR curves for 15% w/w PDMS-Fe<sub>3</sub>O<sub>4</sub> measured at 24.13 GHz with the external field applied parallel ( $\varphi = 0^\circ$ ) or perpendicular ( $\varphi = 90^\circ$ ) to the needles. If no field is applied during the curing of the samples, then both spectra are coincident. (b)  $H_r(\varphi)$  curves for 5% w/w PDMS-Fe<sub>3</sub>O<sub>4</sub> measured at 24.13 GHz. (c) ZFC and FC magnetization vs temperature curves ( $H = 0.01$  T) for the PDMS-Fe<sub>3</sub>O<sub>4</sub> structured composite with a 15% w/w filler concentration: (—●—)  $\varphi = 0^\circ$ ; (—○—)  $\varphi = 90^\circ$ . (d) ZFC and FC magnetization vs temperature curves ( $H = 0.01$  T) for the PDMS-Fe<sub>3</sub>O<sub>4</sub>@Ag structured composite with a 15% w/w filler concentration: (—●—)  $\varphi = 0^\circ$ ; (—○—)  $\varphi = 90^\circ$ .

behavior to that described in Figure 3 for the powders and as explained in section 3.3.

FMR measurements were performed only for PDMS-Fe<sub>3</sub>O<sub>4</sub> MRE. We have studied the dependence of the resonance field and the line width as a function of the angle between the external magnetic field and the orientation of the needles in the composite, where  $\varphi = 0$  and  $90^\circ$  correspond to the field parallel and perpendicular to the needles, respectively (Figure 5a). Variations in the resonance field  $H_r$  as a function of  $\varphi$  are shown in Figure 5b, which follows an almost sinusoidal dependence. No anisotropy was observed in the composites cured in the absence of a magnetic field (random composite). However, a shift of 600 Oe in  $H_r$  between  $\varphi = 0$  and  $90^\circ$  was found for 5% w/w Fe<sub>3</sub>O<sub>4</sub> MRE (about an 8% change in  $H_r$ ). This variation clearly shows that the process of curing the composite in the presence of a magnetic field produces an easy axis parallel to the needles. However, the observed changes in  $H_r$  are considerably lower than those expected from a simplistic model of a perfectly aligned group of needles for which an upper limit of  $H_r(90^\circ) - H_r(0^\circ)$  due to the shape anisotropy is given by  $(3/2)2\pi M_s$  (Butera et al.<sup>39</sup>), which in our case renders 2650 Oe (using  $M_s = 281$  emu/cm<sup>3</sup> obtained from Figure 3a and  $\rho_{\text{bulk}} = 5.2$  g/cm<sup>3</sup>). Because we observed  $H_r(90^\circ) - H_r(0^\circ) \approx 600$  Oe, it follows that the measured anisotropy is considerable lower than that expected from the above simple model. An understanding of the microscopic origin of the measured magnetic anisotropy is beyond the scope of the present work and should consider the effects of magneto-crystalline anisotropy,<sup>40</sup> possible morphology effects, and dipole–dipole interactions among particles.<sup>39</sup>

**3.5. MRE PDMS Composites: Elastic Properties.** Stress versus strain cycles are shown in Figure 6a. It is observed that the MRE composites display elastic behavior with low

hysteresis. Figure 6b shows the responses for different composites that were compressed up to a maximum stress and then strain was kept fixed for 10 s with the observation of a very short relaxation time that is in agreement with the elastic behavior of the MRE composites.

Figure 6c illustrates some examples of the  $L$  versus  $P$  curves that are calculated from the stress–strain analysis, where  $L$  stands generically for the thickness of the sample. These curves were well fitted by exponential decays (Young's law), recovering Young's modulus from the fit. Table 2 shows Young's modulus of the MRE composites measured for the different samples and conditions (e.g., parallel and perpendicular to the needles, composites with random orientation, etc.). The recovered values for Young's modulus of PDMS in the absence of fillers are in agreement with reported values in previous work by other authors<sup>41–45</sup> and with our own previous work.<sup>23,26</sup> These values are also in agreement with those recovered by fitting the stress–strain curves using the Mooney–Rivlin law with five-parameter fitting.<sup>46</sup>

The Young's moduli of the composites in both directions, parallel and perpendicular to the needles, are referred to as  $E_{\parallel}$  and  $E_{\perp}$ , respectively. Values of the percentage elastic anisotropy, defined as  $100 \times (E_{\parallel} - E_{\perp})/E_{\perp}$ , are shown in Table 2. The main aspect to consider is that percentage values larger than 15% are obtained in all cases. An analysis of these results on a microscopic level is beyond the scope of this work, although some aspects can be considered. For example, it is observed that the largest anisotropy is obtained for the 15% Fe<sub>3</sub>O<sub>4</sub> MRE, which is the composite having the largest length and diameter of needles (and the largest volume fraction), as shown in Table 1. Another interesting feature is the excellent agreement with Varga et al.,<sup>15</sup> which is related to the tendency



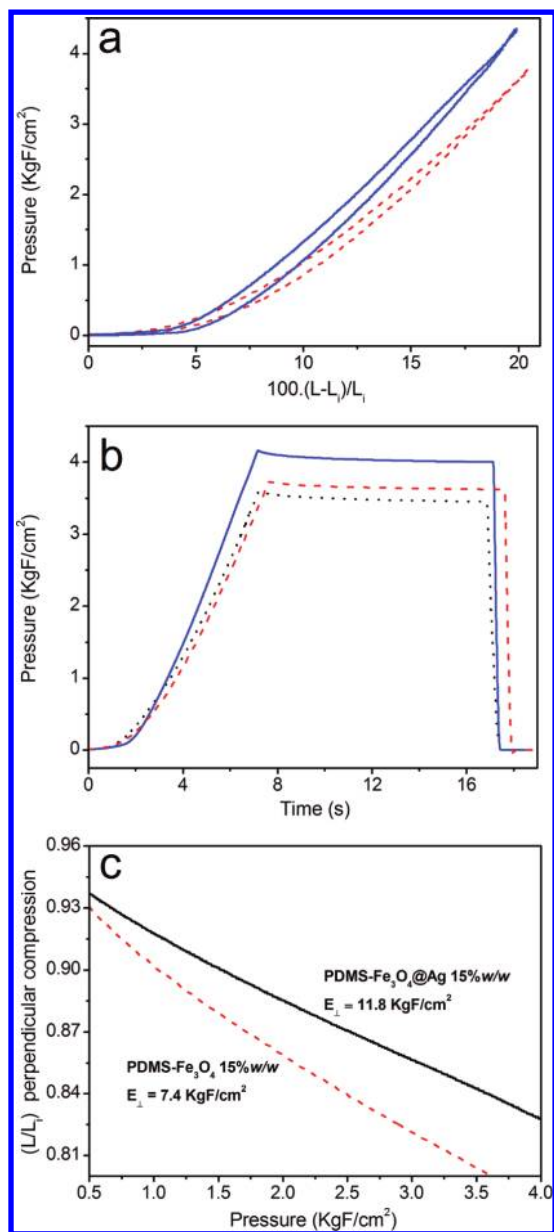


**Figure 6.** (a) PDMS-Fe<sub>3</sub>O<sub>4</sub> composite samples are compressed up to 20% and then decompressed at constant speed: (—) 15% w/w parallel; (---) 15% w/w perpendicular. (b) Relaxation curves (a given sample is compressed up to different maximum stresses and the compression distance is kept fixed for 10 s: (—) 15% w/w parallel; (---) 15% w/w perpendicular; (···) 15% w/w random. (c) Compression curves for a perpendicular 15% w/w PDMS-Fe<sub>3</sub>O<sub>4</sub> composite (---) and a perpendicular 15% w/w PDMS-Fe<sub>3</sub>O<sub>4</sub>@Ag composite (—).

observed in Table 2 for different concentrations of NPs and directions (including random).

We explored the comparison of the recovered Young's modulus with predictions from effective medium theory. For nonstructured composites, the extended Guth–Smallwood model was used, which is a good approximation for comparison purposes in the framework of the EMT.<sup>17,46–49</sup> Specifically, we used eqs 5 and 6 from Coquelle et al.,<sup>46</sup> which predict a value for Young's modulus (referred to as  $E^*$ ) as a function of the filler volume fraction ( $\Phi_v$ ). Those equations were applied to calculate  $E^*$  for the nonstructured PDMS-Fe<sub>3</sub>O<sub>4</sub> with  $\Phi_v = 0.075$ .

**Table 2.** Young's Modulus of the MRE Composites Measured for the Different Samples and Conditions<sup>a</sup>

composite	Young's modulus, kgF/cm <sup>2</sup>	$\{(E_{\parallel} - E_{\perp})/(E_{\perp})\} \times 100$
PDMS	7.0 ± 0.1	
PDMS-Fe <sub>3</sub> O <sub>4</sub> 15% w/w random	5.8 ± 0.2	
PDMS-Fe <sub>3</sub> O <sub>4</sub> 15% w/w	11.1 ± 0.1	50
PDMS-Fe <sub>3</sub> O <sub>4</sub> 15% w/w ⊥	7.4 ± 0.1	
PDMS-Fe <sub>3</sub> O <sub>4</sub> @Ag 15% w/w	14.0 ± 0.2	19
PDMS-Fe <sub>3</sub> O <sub>4</sub> @Ag 15% w/w ⊥	11.8 ± 0.1	
PDMS-Fe <sub>3</sub> O <sub>4</sub> 5% w/w	7.0 ± 0.1	17
PDMS-Fe <sub>3</sub> O <sub>4</sub> 5% w/w ⊥	6.0 ± 0.2	
PDMS-Fe <sub>3</sub> O <sub>4</sub> @Ag 5% w/w	9.2 ± 0.1	15
PDMS-Fe <sub>3</sub> O <sub>4</sub> @Ag 5% w/w ⊥	8.0 ± 0.1	

<sup>a</sup>The recovered Young's moduli of the composites in both directions, parallel and perpendicular to the needles, are referred as  $E_{\parallel}$  and  $E_{\perp}$ , respectively. Values of the percentage elastic anisotropy, defined as  $100 \times (E_{\parallel} - E_{\perp})/E_{\perp}$ , are shown.

Young's modulus and Poisson's ratio of the filler (we used Fe<sub>3</sub>O<sub>4</sub>) appears as parameters and were taken from the literature.<sup>50–52</sup>  $E^* = 8.3$  kgF/cm<sup>2</sup> was obtained from the calculations, and the experimentally recovered value is  $5.8 \pm 0.2$  kgF/cm<sup>2</sup>. The agreement is good considering the several approximations used in the model, such as perfect adhesion between the polymeric matrix and the filler (which is not satisfied in our case) and noninteractive filler particles (unfulfilled for the magnetic particles).

For anisotropic composites (aligned fillers), there are two frequently used models for calculating Young's modulus of composites with aligned fillers having a large shape ratio factor ( $\xi = \text{length}/\text{diameter}$ ): modified Halpin–Tsai equations<sup>17,53,54</sup> and the Hui–Shia model.<sup>55–57</sup> In these models, Young's modulus is calculated as a function of several parameters: the shape ratio factor of the filler ( $\xi$ ), its volume fraction ( $\Phi_v$ ), and Young's modulus of the matrix ( $E_m$ ) and of the filler ( $E_f$ ). The Halpin–Tsai equation allows us to calculate Young's modulus in the direction parallel to the filler alignment,  $E_{\parallel}$ , and the Hui–Shia model predicts  $E_{\parallel}$  and  $E_{\perp}$ . Both models assume perfectly cylindrical fillers, with no interactions between them, that are totally adhered to the polymer matrix. Although these hypotheses can be questioned in the present case, they can be considered to be a first approximation for predictions in terms of the effective medium theory. The central point of discussion refers to the actual values of the shape factor in the systems studied in this work. The needles obtained in our studies are formed by clusters of microparticles (Fe<sub>3</sub>O<sub>4</sub>@Ag) or nanoparticles (Fe<sub>3</sub>O<sub>4</sub>) that form chains when a magnetic field is applied during curing. This leads to needles whose morphology is far from a perfectly cylindrical shape but present narrowing and narrowed ends, which can be interpenetrated by the elastomeric polymer. All of these aspects were observed by SEM. Therefore, the values reported in Table 1, associated with the morphology of the needles, can hardly be used for a microscopic description in the context of the above models. We therefore conducted the following analysis: we used the elastic anisotropy values shown in Table 2 as inputs for the models to

calculate actual values of the form factors. This methodology is analogous to that used by Wu et al.<sup>54</sup> Both models, Halpin–Tsai and Hui–Shia, rendered similar values of the effective  $\xi$ , between 5 and 50 depending on the chemical nature of the filler and the volume fraction in the composite, which are lower than the shape ratio calculated from Table 1 by factors of about 0.1–0.3. Recovering effective lower shape factors is in agreement with the microscopic description of the needles described above. The same tendencies were reported by Wu et al.<sup>54</sup> and Fornes and Paul<sup>57</sup> for other fillers.

Whereas the verification of theoretical models used to calculate elastic parameters or to predict their dependence on the concentration of particles requires a systematic study in which the percentage of fillers is varied over a wide range, which is beyond the scope of this study, the obtained results indicate that the referenced models can be reasonable applied, provided that the microscopic morphology of the fillers (needles in our case) is very well characterized. In this context, some structures similar to the needles-like ones obtained in the present work have been referred to as pseudochains by other authors.<sup>46,49</sup>

**3.6. MRE PDMS Composites: Piezoresistivity and Magnetoresistivity.** Electrical resistivities ( $\Omega\cdot\text{cm}$ ) were measured parallel ( $\rho_{\parallel}$ ) and perpendicular ( $\rho_{\perp}$ ) to the direction of the needles as a function of the applied pressure ( $P$ ) in the absence of a magnetic field. In all cases, the pressure was applied in the same direction in which the electrical conductivity was measured. The variation of  $\rho_{\parallel}$  and  $\rho_{\perp}$  with  $P$  is shown in Figure 7 for different filler percentages. Figure 7a compares  $\rho_{\parallel}$  and  $\rho_{\perp}$  for 15% w/w PDMS- $\text{Fe}_3\text{O}_4$ @Ag. The values of  $\rho_{\parallel}$  are about 10 times lower than those of  $\rho_{\perp}$  at the lowest pressure, and both values converge for pressures higher than 2  $\text{kgF/cm}^2$ . We assign this convergence to the high density of needles in 15% composites (Table 1 and Figure S3, Supporting Information). Figure 7b is an amplification of Figure 7a for  $\rho_{\parallel}$ . Figure 7c illustrates  $\rho_{\parallel}$  for a 5% composite, for which  $\rho_{\perp} = 62 \text{ M}\Omega\cdot\text{cm}$  was obtained. The results of Figure 7 show that anisotropic conduction was obtained and, in the particular case of 5% composites, significant conductivity is obtained only in the direction of the needles ( $\rho_{\perp}/\rho_{\parallel} \approx 10^6$ ). Both resistivities decrease with increasing pressure (in the range of 0–3  $\text{kgF/cm}^2$ ) and were well fitted as a function of  $P$  by exponential decays. (The recovered fitted parameters are discussed in the Discussion.) Therefore, the obtained MRE can be used as pressure sensors having an additional interesting feature of an anisotropic response.

Both resistivities,  $\rho_{\parallel}$  and  $\rho_{\perp}$ , for 5 and 15% composites decrease with the applied magnetic field  $H$  in the range of 0–5000 G at 298 K; see Figure 8 (except for  $\rho_{\perp}$  in 5% composites where no conduction was detected). The  $H$  field was applied in collinear and all perpendicular combinations with respect to the electrical flux,  $J$ . However, it is worth noting that no changes in the current were detected for  $H \perp J$ .

A time between measurements was considered in order to ensure that the system reaches total relaxation. The relaxation curve is shown in Figure 8d for a particular sample. Full relaxation in all cases was obtained 60 s after changing the magnetic field. This relaxation is not influenced by instrumental factors (which were considered during measurements), thus being a physical characteristic of the system related to the whole magnetic–elastic relaxation of the prepared MRE composites.

Figure 9 shows the percentage changes in the electrical conductivities for the different samples and conditions. The dependence on  $H$  was fitted by a simple model described in

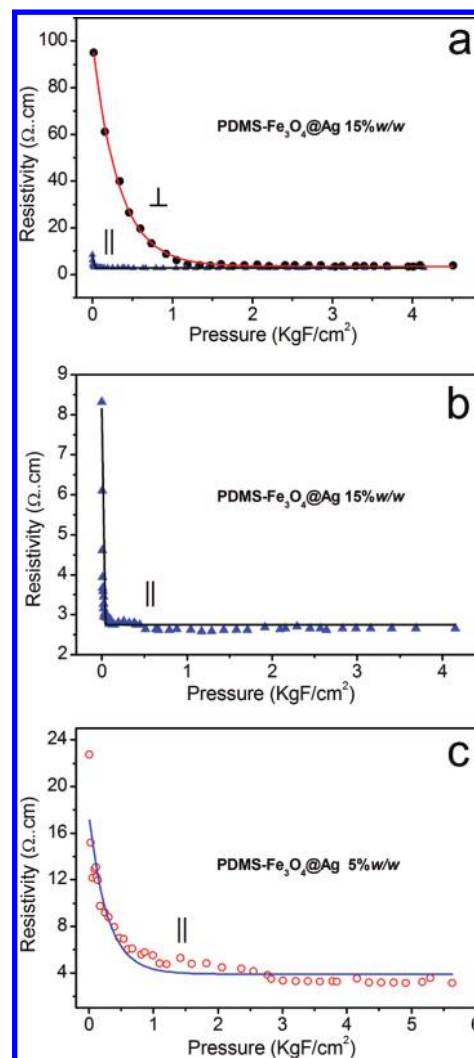


**Figure 7.** (a) Comparison of the piezoresistivity longitudinal ( $\rho_{\parallel}$ ) and transverse ( $\rho_{\perp}$ ) to the direction of the needles in the composite with 15% w/w  $\text{Fe}_3\text{O}_4$ @Ag. (b) Piezoresistivity in the longitudinal direction ( $\rho_{\parallel}$ ) in the composite with 15% w/w  $\text{Fe}_3\text{O}_4$ @Ag. (c) Piezoresistivity in the longitudinal direction ( $\rho_{\parallel}$ ) in the composite with 5% w/w  $\text{Fe}_3\text{O}_4$ @Ag. In all cases, pressure was applied in the same direction in which the electrical conductivity was measured. The solid lines represent the model fit (eq 3 with  $H = 0$ ).

the next section (Discussion). Another aspect is the anisotropic magnetoresistance that is determined as the difference in the magnetoresistances in longitudinal and transverse geometries.

#### 4. DISCUSSION

As indicated by Kchit and Bossis,<sup>19</sup> the conductivity of elastomer composites is mainly governed by the resistance at the interface of contiguous conductive fillers (grains, particles, nanotubes, conglomerates, etc.). In the case of the compressed powder of metal-covered magnetite, the magnetoresistance has been currently assigned to the field-induced alignment of the magnetization of contiguous grains.<sup>58–60</sup> This effect is associated with the intergranular transport of spin-polarized electrons. In this model, the free, partially spin-polarized electrons jump from one silver layer in one agglomerate to one contiguous layer, an activated process whose barrier can be lowered by the external magnetic field  $H$  by avoiding large mismatches in electron spin polarization between silver covers.



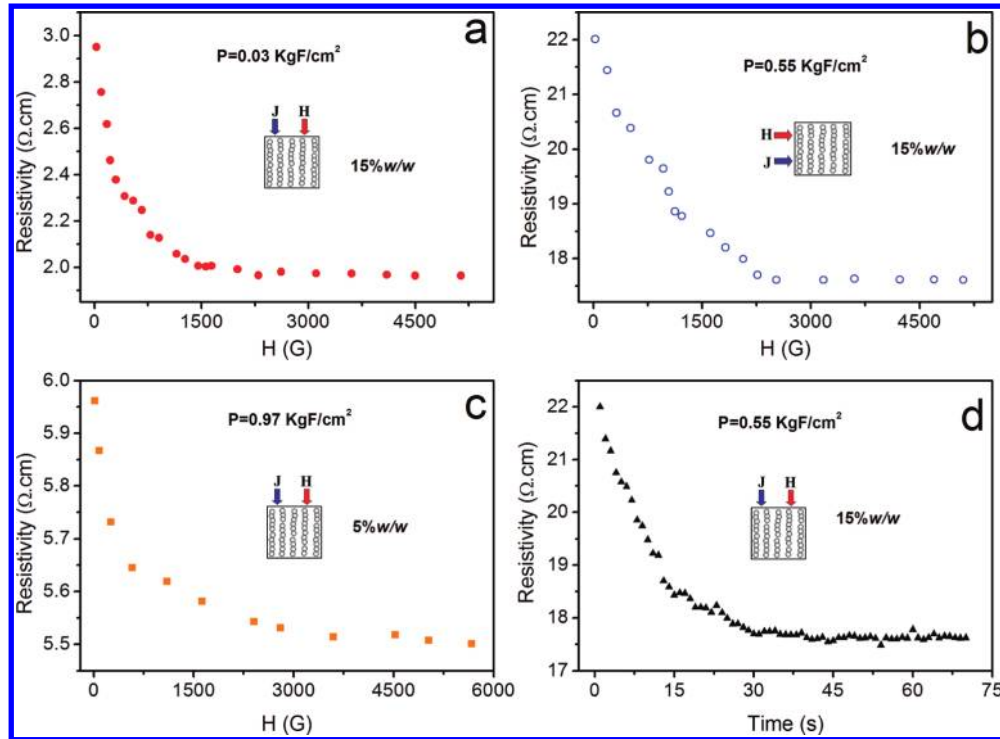


**Figure 8.** PDMS-Fe<sub>3</sub>O<sub>4</sub>@Ag resistivity as a function of the applied magnetic field. (a) Longitudinal resistivity of the PDMS-Fe<sub>3</sub>O<sub>4</sub>@Ag-structured composite with 15% w/w filler concentration and  $P = 0.03 \text{ kgF/cm}^2$ . (b) Transversal resistivity of the PDMS-Fe<sub>3</sub>O<sub>4</sub>@Ag-structured composite with 15% w/w filler concentration and  $P = 0.55 \text{ kgF/cm}^2$ . (c) Longitudinal resistivity of the PDMS-Fe<sub>3</sub>O<sub>4</sub>@Ag-structured composite with 5% w/w filler concentration and  $P = 0.97 \text{ kgF/cm}^2$ . (d) Longitudinal resistivity of the PDMS-Fe<sub>3</sub>O<sub>4</sub>@Ag-structured composite with 15% w/w filler concentration as a function of time ( $P = 0.55 \text{ kgF/cm}^2$ ,  $H = 5300 \text{ G}$ ).  $H$  was collinearly applied with respect to the electrical flux,  $J$ , in all cases. For  $H \perp J$ , no changes in the current were detected.

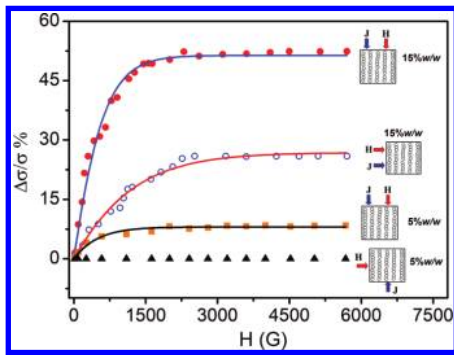


**Figure 9.**  $\Delta\sigma/\sigma\%$  as a function of  $H$  at 298 K for different percentages of Fe<sub>3</sub>O<sub>4</sub>@Ag in the MRE elastomer. The field  $H$  was applied collinearly and at all perpendicular combinations with respect to the electrical flux,  $J$ . No changes in the current were detected for  $H \perp J$ . The solid lines represent the fits to the model (eq 2).

The magnetic field actually induces the partial alignment of the Fe<sub>3</sub>O<sub>4</sub> magnetic moments in the nanodomains, generating a nonrandom distribution of spin-polarized electrons in the two contiguous silver-covered conglomerates, with spins preferentially aligned in the direction of  $H$ .

These effects can be mathematically accounted for by the following proposed model that fits our experimental results, both the piezoresistive and magnetoresistive variations. Here, we assume that the intergrain conduction between silver-covered superparamagnetic grains in the presence of an external magnetic field  $H$  and a pressure  $P$  is considered to be an equivalent electrical model formed by two resistances in series, referred to as  $R_i$  and  $R_H$ . The total intergrain resistance is then

taken to be equal to  $(R_i + R_H)$ . Here,  $R_i$  represents an intergrain resistance accounting for the electron jumps between grains in a polycrystalline material that is considered here to be dependent on  $P$  and independent of  $H$ . The resistance  $R_H$  accounts for the effect of partially matching the average spins of both grains by spin alignment through the presence of  $H$ . These effects can be accounted for by the proposed expression  $R_H \approx \rho_H = B \exp(-\gamma H/kT)$  where  $k$  is the Boltzmann constant.  $B$  and  $\gamma$  are positive constants, thus  $R_H$  decreases with  $H$ . Therefore, the dependence of  $H$  on the total intergrain resistance is given by  $R_i + R_H = R_i + B(l/S) \exp(-\gamma H/kT)$  (where  $B$  is a constant and  $l$  and  $S$  are the length and cross-sectional area of the sample, respectively). Thus, according to this model the measured resistance must be given by

$$R = R_\infty + (R_0 - R_\infty) \exp\left(-\frac{\gamma H}{kT}\right) \quad (1)$$

where  $R_0$  and  $R_\infty$  represent the measured resistance at zero and high magnetic field, respectively, with both being dependent on  $P$ .

The relative percentage changes in conductivity,  $(\Delta\sigma/\sigma)\%$ , as a function of  $H$  can be fitted to an expression derived directly from eq 1

$$\begin{aligned} \frac{\Delta\sigma}{\sigma}\% &\equiv \frac{\sigma(H) - \sigma(H=0)}{\sigma(H=0)} \times 100 \\ &= 100 \times \frac{(\Delta\sigma/\sigma)_\infty \left(1 - \exp\left(-\frac{\gamma H}{kT}\right)\right)}{1 + (\Delta\sigma/\sigma)_\infty \exp\left(-\frac{\gamma H}{kT}\right)} \end{aligned} \quad (2)$$

where  $(\Delta\sigma/\sigma)_\infty$  is the value of the relative change in conductivity at high magnetic field and at the considered pressure.

Excellent fits of the experimental results using eq 2 were obtained, as shown in Figure 9. The recovered values of  $\gamma/kT$  when  $\mathbf{H} \parallel \mathbf{J}$  and both are collinear with the needles are almost identical for 15 and 5% MRE samples  $\{(2.4 \pm 0.1) \times 10^{-3}$  and  $(2.1 \pm 0.3) \times 10^{-3} \text{ G}^{-1}$ , respectively $\}$  and are independent of the pressure  $P$ . These results are excellent indicators of the physical consistence of the model. However, when  $\mathbf{H} \parallel \mathbf{J}$  but both are perpendicular to the needles, a lower value,  $\gamma/kT = (1.0 \pm 0.1) \times 10^{-3} \text{ G}^{-1}$ , was recovered. This is also in agreement with the physical picture as a quantitative indication of the higher magnetic barrier for transporting electrons in the direction perpendicular to the needles. The values of  $(\Delta\sigma/\sigma)_\infty$  are dependent not only on the filler concentration but also on the particular pressure applied to the sample.

Although the fundamentals of magnetoresistivity (MR) effects in the  $\text{Fe}_3\text{O}_4$ -Ag-covered PDMS systems presented here have not yet been systematically investigated from their fundamental and physical bases yet, the origin of MR in other related systems has been ascribed to spin injection between particles due to spin imbalances. For instance, Hu et al.<sup>61</sup> and Hsu et al.<sup>62</sup> observed MR in composite films formed by percolating Ag and  $\text{Fe}_3\text{O}_4$  particles (granular system). In both papers, the authors assume the same physics as in ferromagnetic-metal junctions used in spintronic devices for interpreting the MR effects:<sup>63</sup> coupling between charge and spin at the interface between  $\text{Fe}_3\text{O}_4$  and Ag with spin injection into Ag granules. The imbalance of spin-polarized conduction electrons predicts the observed magnetoresistance effects when a magnetic field is applied and aligns the magnetic moments of  $\text{Fe}_3\text{O}_4$ , thus the spin-polarized current causes a nonequilibrium-induced magnetization in the Ag granules. The spin diffusion length of Ag was later estimated to be 11 nm at room temperature<sup>64</sup> but much shorter for Al, although some of the experimental results must be taken with care.<sup>65</sup> In our system, a layer of about 18 nm between silver-covered microparticles is obtained if about  $10^3$  60–100 nm spherical  $\text{Fe}_3\text{O}_4$  clusters are formed inside each microparticle (although these are raw estimations based on oversimplified arguments, bulk densities, etc.). This kind of structure, where several clusters of ferromagnetic particles with a silver cover thin enough to provide spin-polarization effects, can explain the MR observed effects. It is worth mentioning that we paid special attention to the possibility of observing elastic deformations when applying the magnetic fields, which may induce the approach of the polymer chains, increasing the percolation probability and therefore providing higher electrical conduction. This type of effect was observed in systems much more elastic than ours.<sup>66</sup> In this work, elastic deformations produced by applying magnetic fields were not observed, even for a 6500 G field, which is greater than those used in the MR experiments. Therefore, that possibility is discarded as an explanation of the MR behavior in our elastomers. The proposed model in this article, in which the activation barrier between grains decreases in the presence of a magnetic field and is associated with spin-polarization effects, quantitatively explains all of the presented results and consistently adjusts the dependence of the electrical conductivity with the magnetic field applied in the considered range.

In addition, it must be remarked that in our materials the inhomogeneity is provided by aligned millimeter needles of silver-covered  $\text{Fe}_3\text{O}_4$  nanoparticles in an elastomeric polymer. This requires a consideration of the percolation of the needles

under a given strain, which is the reason that the conductivity increases with applied pressure,  $P$  (Figure 7). Percolation provides the piezoresistivity effects ( $R = R(P)$ ), which in our MRE also have anisotropic properties. We assume that this effect is taken into account in our model by introducing an exponential dependence of  $R_i$  on  $P$ , which is consistent with the experimental results shown in Figure 7. Therefore, the fully extended model that simultaneously considers the piezoelectric and the magnetoresistivity properties must be written as follows

$$\rho_k(T, P, \mathbf{H}) = A_k(T) \exp\left(-\alpha_k \frac{P}{E_k}\right) + B_k \exp\left(-\frac{\gamma_k \mathbf{H}}{kT}\right) \quad (3)$$

where the subscript  $k$  stands for the direction  $\perp$  or  $\parallel$  with respect to the needles;  $A_k(T)$  is dependent only on the temperature  $T$ ;  $E_k$  represents Young's modulus; and  $B_k$ ,  $\alpha_k$ , and  $\gamma_k$  are dependent only on the composition of the MRE (filler concentration). All of these parameters can be recovered from the performed experiments (Figures 6–8) and are shown in Table 3.

**Table 3. Recovered Fit Parameters from Figures 7 and 9 Using Equation 3<sup>a</sup>**

% w/w and direction of $\mathbf{J}$ with respect to the needles	$\gamma/kT, \text{G}^{-1}$	$A, \Omega\text{-cm}$	$B, \Omega\text{-cm}$	$\alpha$
15 $\parallel$	$(2.4 \pm 0.1) \times 10^{-3}$	$5.4 \pm 0.2$	$2.8 \pm 0.1$	$180 \pm 10$
15 $\perp$	$(1.0 \pm 0.1) \times 10^{-3}$	$96.4 \pm 0.8$	$3.4 \pm 0.2$	$3.1 \pm 0.1$
5 $\parallel$	$(2.1 \pm 0.3) \times 10^{-3}$	$13.1 \pm 0.8$	$4.0 \pm 0.3$	$21 \pm 3$

<sup>a</sup>All values correspond to measurements performed for the PDMS- $\text{Fe}_3\text{O}_4$ @Ag composite at 298 K.

The tendencies observed in Table 3 can be interpreted by considering the structural anisotropy of the samples and the data in Tables 1 and 2. For instance, the parameter  $A + B$ , the intrinsic resistivity in the absence of  $P$  and  $\mathbf{H}$ , is 12 times larger in the perpendicular direction than in the parallel direction for the same amount of filler (15% w/w), in agreement with the observed morphological anisotropy (Table 1), whereas for the parallel direction  $A + B$  decreases with the concentration of fillers, as expected. The same tendency can be observed for  $E/\alpha$ , which represents the characteristic pressure decay associated with the percolation using the values of  $\alpha$  from Table 3 and  $E$  from Table 2.

## 5. CONCLUSIONS

By preparing  $\text{Fe}_3\text{O}_4$ @Ag-PDMS magnetorheological materials, we were able to obtain superparamagnetic and electrically conductive materials with anisotropic properties at room temperature. The main effect was observed in the magnetoresistance, although anisotropic effects were also obtained for the elastic, piezoelectric, and magnetic properties. The magnetoresistance and the piezoelectric properties were explained by a developed model based on a simple physical hypothesis that accounts for all of the relevant physical properties: the hardness of the material ( $E$ ), the direction of the applied pressure, the filler concentration, and the morphological anisotropy induced by the preparation method.

It is important to note that magnetically resistive and piezo-resistive elastic composites were obtained using superparamagnetic particles. Thus, is not indispensable to use ferromagnetic or ferrimagnetic particles, broadening the spectrum of possibilities when designing devices. All of the reported information is of high relevance when designing new materials for devices in flexible electronics, such as sensors or organic-based connectors, one of the most challenging issues nowadays in materials science.

## ■ ASSOCIATED CONTENT

### ■ Supporting Information

Photographs of  $\text{Fe}_3\text{O}_4$  nanoparticle and  $\text{Fe}_3\text{O}_4@\text{Ag}$  particle (set B) samples. TEM image of  $\text{Fe}_3\text{O}_4$  nanoparticles. Histogram of  $\text{Fe}_3\text{O}_4$  nanoparticle diameters determined on the basis of the TEM image. SEM image of  $\text{Fe}_3\text{O}_4@\text{Ag}$  microparticles. Histogram of  $\text{Fe}_3\text{O}_4@\text{Ag}$  particle (set B) diameters determined on the basis of the SEM image. SEM images of the structured 15% w/w PDMS- $\text{Fe}_3\text{O}_4@\text{Ag}$  composite of  $\text{Fe}_3\text{O}_4@\text{Ag}$  (top and lateral views with respect to the needles). This material is available free of charge via the Internet at <http://pubs.acs.org>.

## ■ AUTHOR INFORMATION

### Corresponding Author

\*E-mail: [rmn@qi.fcen.uba.ar](mailto:rmn@qi.fcen.uba.ar). Tel: xx54-11-4576-3358. Fax: xx54-11-4576-3341.

### Notes

The authors declare no competing financial interest.

## ■ ACKNOWLEDGMENTS

G.J., A.B., P.S.A., and R.M.N. are research members of the National Council of Research and Technology (CONICET, Argentina). J.L.M. is an undergraduate fellow of the University of Buenos Aires (UBA). M.M.R. is a Ph.D. student with a fellowship from CONICET. Financial support was received from the University of Buenos Aires (UBACyT 2008-2010, project X157) and CONICET (PIP 6382). We thank the Center of Advanced Microscopy (CMA) and the Center of Documental Production (CePro) at the School of Sciences (UBA) for allowing us to obtain the presented images and pictures.

## ■ REFERENCES

- (1) Wettels, N.; Santos, V. J.; Johansson, R. S.; Loeb, G. E. *Adv. Rob.* **2008**, *22*, 829–849.
- (2) Katragadda, R. B.; Xu, Y. *Sens. Actuators, A* **2008**, *143*, 169–174.
- (3) Yang, Y.-J.; Cheng, M.-Y.; Chang, W.-Y.; Tsao, L.-C.; Yang, S.-A.; Shih, W.-P.; Chang, F.-Y.; Chang, S.-H.; Fan, K.-C. *Sens. Actuators, A* **2008**, *143*, 143–153.
- (4) Mannsfeld, S. C. B.; Tee, B. C.-K.; Stoltenberg, R. M.; Chen, C. V. H.-H.; Barman, S.; Muir, B. V. O.; Sokolov, A. N.; Reese, C.; Bao, Z. *Nat. Mater.* **2010**, *9*, 859–864.
- (5) Takei, K.; Takahashi, T.; Ho, J. C.; Ko, H.; Gillies, A. G.; Leu, P. W.; Fearing, R. S.; Javey, A. *Nat. Mater.* **2010**, *9*, 821–826.
- (6) Sundar, V. C.; Zaumseil, J.; Podzorov, V.; Menard, E.; Willett, R. L.; Someya, T.; Gershenson, M. E.; Rogers, J. A. *Science* **2004**, *303*, 1644–1646.
- (7) Promislow, J. H. E.; Gast, A. P. *Langmuir* **1996**, *12*, 4095–4102.
- (8) Climent, E.; Maxey, M. R.; Karniadakis, G. E. *Langmuir* **2004**, *20*, 507–513.
- (9) López-López, M. T.; Gomez-Ramirez, A.; Duran, J. D. G.; Gonzalez-Caballero, F. *Langmuir* **2008**, *24*, 7076–7084.
- (10) Wang, J.; Scampicchio, M.; Laocharoensuk, R.; Valentini, F.; González-García, O.; Burdick, J. J. *Am. Chem. Soc.* **2006**, *128*, 4562–4563.
- (11) Mefford, O. T.; Carroll, M. R. J.; Vadala, M. L.; Goff, J. D.; Mejia-Ariza, R.; Saunders, M.; Woodward, R. C., St.; Pierre, T. G.; Davis, R. M.; Riffe, J. S. *Chem. Mater.* **2008**, *20*, 2184.
- (12) Lappas, A.; Zorko, A.; Wortham, E.; Das, R. N.; Giannelis, E. P.; Cevc, P.; Arc, D. *Chem. Mater.* **2005**, *17*, 1199.
- (13) Filipcsei, G.; Csetneki, I.; Szilágyi, A.; Zrínyi, M. *Adv. Polym. Sci.* **2007**, *206*, 137–189.
- (14) Varga, Z.; Filipcsei, G.; Zrínyi, M. *Polymer* **2005**, *46*, 7779–7787.
- (15) Varga, Z.; Filipcsei, G.; Zrínyi, M. *Polymer* **2006**, *47*, 227–233.
- (16) Farshad, M.; Benine, A. *Polym. Test.* **2004**, *23*, 347–353.
- (17) Denver, H.; Heiman, T.; Martin, E.; Gupta, A.; Borca-Tasciuc, D.-A. *J. Appl. Phys.* **2009**, *106*, 064909.
- (18) Jacobo, S. E.; Apesteguy, J. C.; Lopez Antón, R.; Schegoleva, N. N.; Kuryandskaya, G. V. *Eur. Polym. J.* **2007**, *43*, 1333–1346.
- (19) Kchit, N.; Bossis, G. *J. Phys.: Condens. Matter.* **2008**, *20*, 204136.
- (20) Lanotte, L.; Ausanio, G.; Hison, C.; Iannotti, V.; Luponio, C. *Sens. Actuators, A* **2003**, *106*, 56–60.
- (21) Keshoju, K.; Sun, L. *J. Appl. Phys.* **2009**, *105*, 023515.
- (22) Record, P.; Popov, C.; Fletcher, J.; Abraham, E.; Huang, Z.; Whatmore, R. *Sens. Actuators, B* **2007**, *126*, 344–349.
- (23) Antonel, P. S.; Jorge, G.; Perez, O. E.; Butera, A.; Leyva, A. G.; Negri, R. M. *J. Appl. Phys.* **2011**, *110*, 043920.
- (24) Ambrosetti, G.; Johnner, N.; Grimaldi, C.; Maeder, T.; Ryser, P.; Danani, A. *J. Appl. Phys.* **2009**, *106*, 016103.
- (25) Johnner, N.; Grimaldi, C.; Maeder, T.; Ryser, P. *Phys. Rev. E* **2009**, *79*, 020104.
- (26) Negri, R. M.; Rodriguez, S. D.; Bernik, D. L.; Molina, F. V.; Pilosof, A.; Pérez, O. *J. Appl. Phys.* **2010**, *107*, 113703.
- (27) Wan, C.; Zhang, X.; Gao, X.; Wang, J.; Tan, X. *Nature* **2011**, *477*, 304–307.
- (28) Ziese, M.; Blythe, H. J. *J. Phys.: Condens. Matter.* **2000**, *12*, 13.
- (29) Coey, J. M. D.; Berkowitz, A. E.; Balcells, L.; Putris, F. F.; Parker, F. T. *J. Appl. Phys. Lett.* **1998**, *72*, 734–736.
- (30) Senapati, K.; Blamire, M. G.; Barber, Z. H. *Nat. Mater.* **2011**, *10*, 849–852.
- (31) Lua, Z. L.; Xu, M. X. *J. Appl. Phys. Lett.* **2007**, *91*, 102508.
- (32) Garza-Navarro, M.; Torres-Castro, A.; González, V.; Ortiz, U.; de La Rosa, E. *J. Solid State Chem.* **2010**, *183*, 99–104.
- (33) Mandal, M.; Kundu, S.; Ghosh, S. K.; Panigrahi, S.; Sau, T. K.; Yusuf, S. M.; Pal, T. *J. Colloid Interface Sci.* **2005**, *286*, 187–194.
- (34) Iglesias-Silva, E.; Rivas, J.; Isidro, L. M. L.; Lopez-Quintela, M. A. *J. Non-Cryst. Solids.* **2007**, *353*, 829–831.
- (35) Yin, Y.; Li, Z. -Y.; Zhong, Z.; Gates, B.; Xia, Y.; Venkateswaranc, S. *J. Mater. Chem.* **2002**, *12*, 522–527.
- (36) Yaryura, P.; Cordon, G.; Leon, M.; Kerber, N.; Pucheu, N.; Rubio, G.; García, A.; Lagorio, M. G. *J. Agron. Crop Sci.* **2009**, *195*, 186–196.
- (37) Knobel, M.; Nunes, W. C.; Socolovsky, L. M.; De Biasi, E.; Vargas, J. M.; Denardin, J. C. *J. Nanosci. Nanotechnol.* **2008**, *8*, 2836–2857.
- (38) Wang, L.; Luo, J.; Maye, M. M.; Fan, Q.; Rendeng, Q.; Engelhard, M. H.; Wang, C.; Lin, W.; Zhong, C. J. *J. Mater. Chem.* **2005**, *15*, 1821–1832.
- (39) Butera, A. *Eur. Phys. J. B* **2006**, *52*, 297–303.
- (40) Goya, G. F.; Berquo, T. S.; Fonseca, F. C.; Morales, M. P. *J. Appl. Phys.* **2003**, *94*, 3520.
- (41) Carmona, F.; Canet, R.; Delhaes, P. *J. Appl. Phys.* **1987**, *61*, 2550.
- (42) Lee, D.-W.; Choi, Y.-S. *Microelectron. Eng.* **2008**, *85*, 1054–1058.
- (43) Inglis, D. W. *Biomicrofluidics* **2010**, *4*, 026504.
- (44) Tong, J.; Simmons, C. A.; Yu, S. J. *Micromech. Microeng.* **2008**, *18*, 037004.
- (45) Cheng, Q.; Sun, Z.; Meininger, G. A.; Almasri, M. *Rev. Sci. Instrum.* **2010**, *81*, 106104.



- (46) Coquelle, E.; Bossis, G.; Szabo, D.; Giulieri, F. *J. Mater. Sci.* **2006**, *41*, 5941–5953.
- (47) Smallwood, H. M. *J. Appl. Phys.* **1944**, *15*, 758.
- (48) Guth, E. *J. Appl. Phys.* **1945**, *16*, 20.
- (49) Lu, X.; Qiao, X.; Watanabe, H.; Gong, X.; Yang, T.; Li, W.; Sun, K.; Li, M.; Yang, K.; Xie, H.; Yin, Q.; Wang, D.; Che, X. *Rheol. Acta* **2012**, *51*, 37–50.
- (50) Chicota, D.; Mendoza, J.; Zaouia, A.; Louisa, G.; Lepinglea, V.; Roudeta, F.; Lesage, J. *Mater. Chem. Phys.* **2011**, *129*, 862–870.
- (51) Gercek, H. *Int. J. Rock Mech. Miner. Sci.* **2007**, *44*, 1.
- (52) Gerward, L.; Staun Olsen, J. *Appl. Radiat. Isot.* **1995**, *46*, 553.
- (53) Halpin, J. C.; Kardos, J. L. *Polym. Eng. Sci.* **1976**, *16*, 344.
- (54) Wu, Y.-P.; Jia, Q.-X.; Yu, D.-S.; Zhang, L.-Q. *Polym. Test.* **2004**, *23*, 903–909.
- (55) Tandon, G. P.; Weng, G. *J. Polym. Compos.* **1984**, *5*, 327–333.
- (56) Hui, C. Y.; Shia, D. *Polym. Eng. Sci.* **1998**, *38*, 774–782.
- (57) Fornes, T. D.; Paul, D. R. *Polymer* **2003**, *44*, 4993–5013.
- (58) Ziese, M.; Bollero, A.; Panagiotopoulos, I.; Moutis, N. *Phys. Rev. B* **2005**, *72*, 024453.
- (59) Lee, S.; Wang, H. Y.; Shraiman, B. I.; W. Ratcliff, D., II; Cheong, S. W. *Phys. Rev. Lett.* **1999**, *82*, 4508–4511.
- (60) Allia, P.; Bretcanu, O.; Vernè, E.; Celegato, F.; Coisson, M.; Tiberto, P.; Vinai, F.; Spizzo, F.; Tamisari, M. *J. Appl. Phys.* **2009**, *105*, 083911.
- (61) Hu, X.; Xu, M.; Cui, X.; Shang, S. *Solid State Commun.* **2007**, *142*, 595–599.
- (62) Hsu, J.-H.; Chen, S.-Y. *J. Magn. Magn. Mater.* **2002**, *242–245*, 479–481.
- (63) Johnson, M. *Phys. Rev. Lett.* **1991**, *67*, 3594.
- (64) Hsu, J.-H.; Chen, S.-Y.; Chang, W.-M.; Jian, T. S.; Chang, C.-R. *J. Appl. Phys.* **2003**, *93*, 7702.
- (65) Kimishima, Y.; Yamada, W.; Uehara, M.; Asaka, T.; Kimoto, K.; Matui, Y. *Mater. Sci. Eng., B* **2007**, *138*, 69–73.
- (66) Bica, I. *J. Ind. Eng. Chem.* **2010**, *16*, 359–363.